ICAS 2021 SHANGHAI
International Council of the Aeronautical Sciences
32nd Congress of the International Council of the Aeronautical Sciences
September 6-10, 2021 Pudong Shangri-La, Shanghai, China

Numerical Simulation of a Bio-Inspired Flexible Flapping-wing Based on Experimental Measured Deformation

Xiaowu Yang, Yang Pei, Wenqing Yang, Peng Nian, Bifeng Song
School of Aeronautics, Northwestern Polytechnical University, Xi'an, 710072, P.R.China
Phone: +0086 15091185257 Fax: +0086 029 88493278 Email: 915505251@qq.com

Abstract

The force-generation mechanism of a flexible flapping wing was studied by numerical simulation and experiment. To obtain the real deformation pattern of the flapping wing, the photogrammetry technology was used to measure the dynamic deformation of the wing. The dynamic deformation data were subsequently interpolated and embedded into the Computational Fluid Dynamics (CFD) solver to account for the aeroelastic effects. For comparison purposes, a rigid flapping-wing configuration is also simulated. The results show that wing flexibility is beneficial for the thrust generation and provide more flow details of the unsteady aerodynamics of the flapping wing in terms of vortex formation and evolution.

Keywords: Flapping-wing Micro Aerial Vehicles; Photogrammetry; Computational Fluid Dynamics;

1. Introduction

Recent advances in compact electronics and power storage have created an opportunity to mount miniature surveillance equipment on small flying aircraft known as micro air vehicles (MAVs). These micro air vehicles could be used for military missions such as reconnaissance, into hostile territory, scouting, as well as civilian applications such as telecommunications, news broadcasting, crop monitoring, remote sensing, and so on. The flapping-wing MAVs, inspired by natural flyers, have attracted considerable attention on account of their excellent maneuverability and flight capabilities at the Reynolds-number range of $10^3 < Re < 10^5$, which is of most interest to MAV, UAV, and low-speed flight designers.

From conventional military to commercial and civilian, the growing interest in Micro Air Vehicles (MAVs) has given a huge boost to the exploration of unconventional and novel technologies to meet increasingly demanding new requirements. As a subset of the MAVs, Flapping-Wing Micro Air Vehicles (FWMAVs) have attracted intense interest due to their potential applications in civilian and military. FWMAVs can achieve extraordinary flight performance at the low-Reynolds-number regime and in narrow spaces,[1] showing high maneuverability and agility. The reason that FWMAVs can have such high performance is that they can take the advantage of several unsteady aerodynamic effects adopted by natural flyers, such as the clap-and-fling mechanism[2], wake capture[3], and delayed stall[4].

Driven by the desire to replicate the flying creatures' flight abilities, breakthroughs have been made in the development of FWMAVs. In 2011, the Nano Hummingbird[5], the first palm-size tailless FWMAV, was unveiled by AeroVironment. In 2013, Ma et al.[6] built an 80-milligram, insect-scale, flapping-wing robot that mimicked the morphology of flies by using a modular approach to flight control that relies on limited information about the robot's dynamics. In 2018, the Delft University of Technology developed an agile FWMAV, namely, the DelFly Nimble[7], which was equipped with two pairs of wings. The wings exhibit a clap-and-fling motion during the flapping motion, which enables the wings to generate more lift than a single pair of wings[8]. In 2019, Dong et al.[9] developed a new type of air vehicle that was different from the conventional flapping wing air vehicle. The vehicle uses flapping to generate a spin moment, which causes the wing to start spinning, and the spin and flapping together generate the forces required for flight. In 2020, Chen et al[10]. conducted experimental and computational efforts to gain a reliable topology optimization method for the bottom of the trans-mission system. They presented a dynamic simulation modeling method based on the constitutive model of ultraviolet curable resin and nonlinear dynamic characteristics of the transmission system.

There are many studies on the aerodynamic characteristics of flapping wings. Yang et al[11,12]. investigated the aerodynamic performance of a flapping wing by using preconditioned Navier-Stokes equations and the chimera grid method. Xue et al.[13, 14] explored the flapping wing flight by using a coupled Computational Fluid Dynamics (CFD) and Computational Structural Dynamics (CSD) method. Zhou et al.[15,16] focused on the unsteady aerodynamic forces of plunging airfoils. Li et al.[17] analysed the individual influence of pitching and plunging motions on flow structures by changing the phase lag between the geometrical angle of attack and the plunging angle of attack. They found that the plunging motion contributes to the development of the leading edge shear layer, while the pitching motion is the key reason for the instability of the leading edge shear layer. Lang et al.[18] studied the aerodynamic performance of owl-like airfoil undergoing flapping kinematics which were obtained experimentally.

However, the force characteristics of flapping wings can not be accurately revealed by using two-dimensional models or prescribed kinematics. Besides, when the fluid-structure interaction (FSI) technique is used to solve the flow field around the flexible flapping wing, the structure of the flapping wing needs to be modeled. The flapping wing is composed of highly flexible membranes and anisotropic carbon skeletons. During flapping, the wing membrane will be strained, relaxed, and wrinkled. The complicated deformation pattern of the wing membrane makes it difficult to simulate it accurately. As an alternative approach, the real morphological deformation data of the wing can be obtained experimentally by using the photogrammetry technique.[8,19] Then, the real morphological deformation data are taken as input to account for the aeroelastic effect in the CFD simulation. Note that, by doing so, the structural modeling will not be necessary since the morphological deformation data of the wing structure is measured beforehand. Although many researchers have used this mixed experimental-numerical approach to study the aerodynamic characteristics of birds or insects, there are relatively few studies on FWMAVs with this approach.

In the current study, a dovelike FWMAV, developed by the Northwestern Polytechnical University (NPU) was studied. The dynamic deformation data of the wing is obtained by the Digital Image Correlation (DIC) technique. The dynamic deformation data then can be used for the calculation of aerodynamic forces. In the calculation of aerodynamic forces, the dynamic deformation data is taken as input to account for the aeroelastic effect in the CFD simulation. The deformation characteristics of the wing are represented by the dynamic deformation data, which in principle excludes the modeling of the complex flapping-wing structure.

This paper is organized as follows: firstly, the dynamic deformation data were obtained experimentally by the DIC technique. Then, the dynamic morphological model of the flapping wing is acquired by interpolation of the experimental data. Further, the dynamic morphological model was embedded into the CFD solver to obtain the aerodynamic force and flow structure of the flapping wing in a real deformation pattern.

2. Materials and methods

2.1 Flapping mechanism

The flexible wings were connected to a four-bar mechanism (Figure 1a). The four-bar mechanism was driven by a Faulhaber servo motor, which can drive the flapping mechanism with high precision.

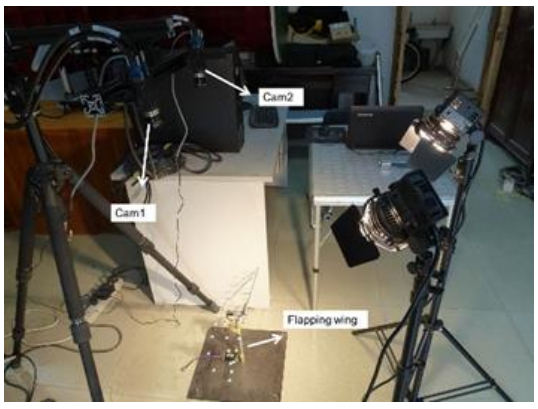

(a)Experimental setup

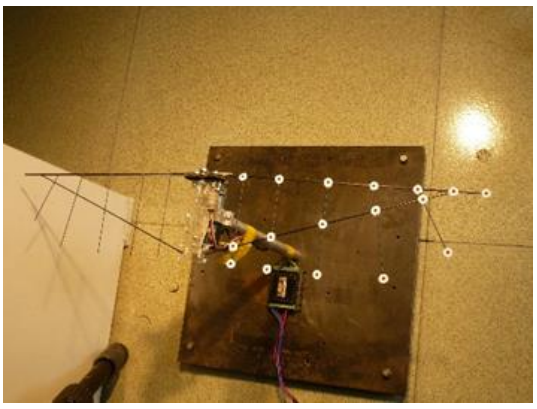

(b)Markers on the wing

Figure 1 – Experimental setup and markers on the wing.

2.2 Wing deformation measurement

To obtain the actual morphological deformation data, several representative points were marked on the wing (Figure 1b). The markers were instantaneously traced via a photogrammetry system (Figure 1a), in which two high-speed cameras, indicated as Cam1 and Cam2, were used to record the wing markers.

The photogrammetry technology is quite suitable for the measurement of flapping wing deformation due to its nature of image correlation, thus have no interference to the test subject. It has two synchronized high-speed cameras that align with each other by a certain angle. The angle is carefully adjusted that ensure the flapping wing lies in the viewport of both cameras. To ensure sufficient light supply, two halogen lamps that emit uniform and powerful white light are used to illuminate the flapping wing.

Before the measurement, the two cameras need to be calibrated. As shown in Figure 2, a series of images of the calibration grid need to be acquired before calibration. For a typical setup, 15-20 images will be a good number. For each image, a number of points extracted is displayed. When the extraction is complete, the calibration will be computed; a score will be displayed for each image; and a final score displayed in the lower right. After the calculation is complete, you will be presented with a report of calibration results and error scores. The errors will be displayed per image, as well as an overall error score. Below the calibration scores, the intrinsic parameters of the two cameras and their relative position information are listed. Each result is listed with a confidence interval that indicate the quality of the image sequence. When the error score and confidence intervals are acceptable, the calibration is complete.

Point tracking is carried out manually by the operator. Thus, beside the accuracy of camera calibration, the accuracy of the measurement is also related to the operator. If the camera calibration error and human tracking error are not taken into account, then according to the 2048×1088 pixels resolution of the cameras and the 25×50cm size of the field of view, it can be calculated that the measurement error of the system is 0.23mm.

Once calibration is complete, the camera model (the intrinsic parameters of the two cameras and their relative position information) is built. The displacement of the marker can be calculated by substituting the pixel coordinates of the marker on the two cameras into the previously obtained camera model.

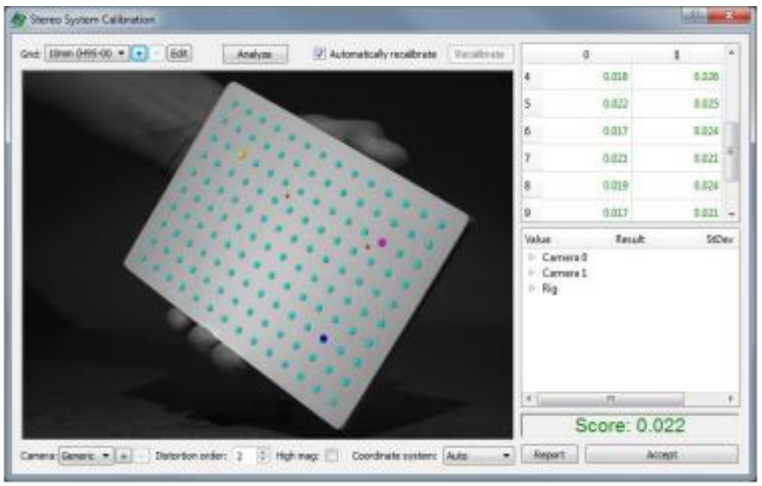

Figure 2 – Camera calibration.

2.3 Reconstruction of the wing surface

The reconstruction of the wing surface at a certain time instant (t/T = 0.0) is illustrated in Figure 3. After obtaining the coordinates of the marked points (Figure 3a), the points were then connected by spline curves, and the spline curves were further interpolated by multisection surface to obtain the wing surface(Figure 3b). A similar operation was performed at all instants to obtain the wing morphology within a flapping cycle as shown in Figure 4.

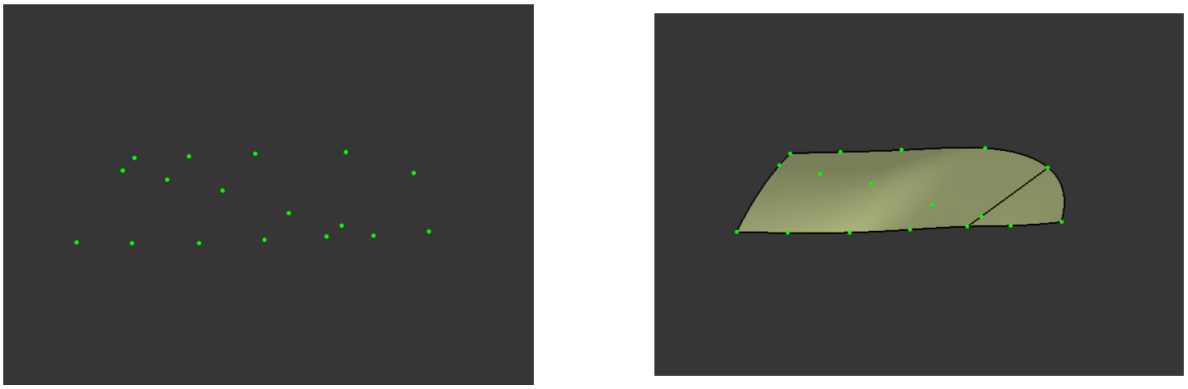

(a) marker points from photogrammetry measurement

(b) reconstructed wing surface

Figure 2 – Wing surface reconstruction: (a) marker points; (b) reconstructed wing surface.

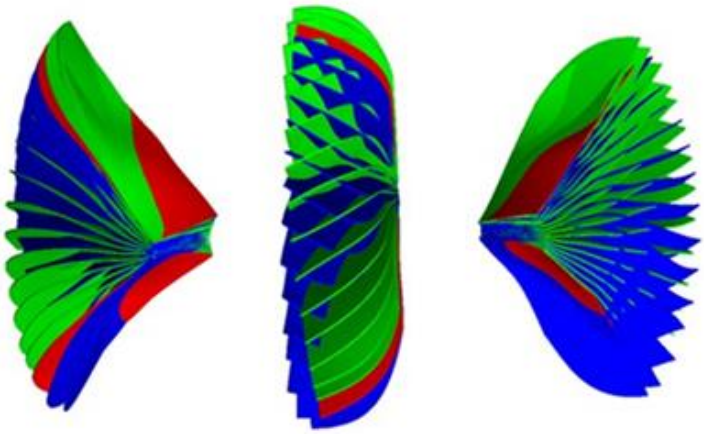

Figure 4 – The morphology of the wing surface at different instants (downstroke in green, upstroke in blue, and red in the reversal stage).

2.4 Numerical method and setup

The unsteady viscous flow generated by the flexible wing was numerically simulated by Ansys Fluent. The simulation solves the full laminar flow due to the relatively low Reynolds number. The pressure-based solver was employed to cope with the incompressible low-speed flows existing in the current study. The coupled algorithm was chosen for the pressure-velocity coupling. In the spatial discretization, least-squares cell-based, second-order, and second-order upwind were used for the gradient, pressure, and momentum respectively. The first order implicit was applied for the transient formulation.

After the wing surface at t/T=0.0 was reconstructed, the surface mesh used for CFD simulation was generated on the reconstructed wing surface at this instant. The surface mesh was further transferred to the remaining time instants by the Radial Basis Function (RBF) based on the coordinates of the markers of the corresponding time instants. Note that, only the surface mesh was transferred, the deformation of the interior mesh was accomplished by the dynamic mesh algorithm[20].

The sampling frequency of the cameras is at 200Hz. The flapping frequency was 6Hz. This yields 34 time instants within one flapping cycle, which are not sufficient to temporally resolve the flow-structure evolution during the flapping motion. The Fourier series fitting with 8th order was used to perform a temporal interpolation to obtain sufficient temporal resolution for the CFD simulation. The 34 sets of the coordinate data of the surface mesh node within one flapping cycle were interpolated to 500 equidistant time moments by sampling from the fitted model.

During the simulation, the wing undergoes substantial rigid body rotation and structural deformation. This configuration challenges the existing dynamic mesh algorithms because the mesh

near the wing will experience large distortion and twists which can easily result in negative cell volume, thus abort the solver. Given this difficulty, the overset mesh strategy was adopted. Figure 5 shows the computational mesh zones and the overset mesh strategy. Because the flexible wings are symmetrical with respect to the fuselage, only one side of the wings was simulated. A symmetry plane was applied where the middle of the body would be. There are two mesh zones in total, i.e., the component mesh zone (with the wing wrapped inside) and the background mesh zone (with dense mesh region that wraps the range of flapping). The background mesh and the component mesh have a similar cell size at the overset interface to facilitate accurate data transfer. The size of the background mesh zone and the component mesh zone are 30c × 30c × 30c and 5c × 5c × 5c respectively. The background mesh has a fine mesh region that covers the flapping range of the overset mesh. Note that, during the simulation, the wing undergoes remarkable rigid body rotation and structural deformation. In view of this, the component mesh was set to exhibit the same rigid rotation of the wing to counteract the distortion of the mesh caused by the rigid flapping of the wing. Therefore, the component mesh only needs to deal with the mesh distortion caused by structural deformation, which is much moderate than the distortion caused by rigid rotation.

For comparison purposes, a rigid flapping-wing configuration is also simulated. Since the freestream velocity is zero, the Reynolds-number is defined by the chord length of the wing root and the maximum linear velocity of the wing tip. A UDF (user-defined function) was used to update the wing mesh.

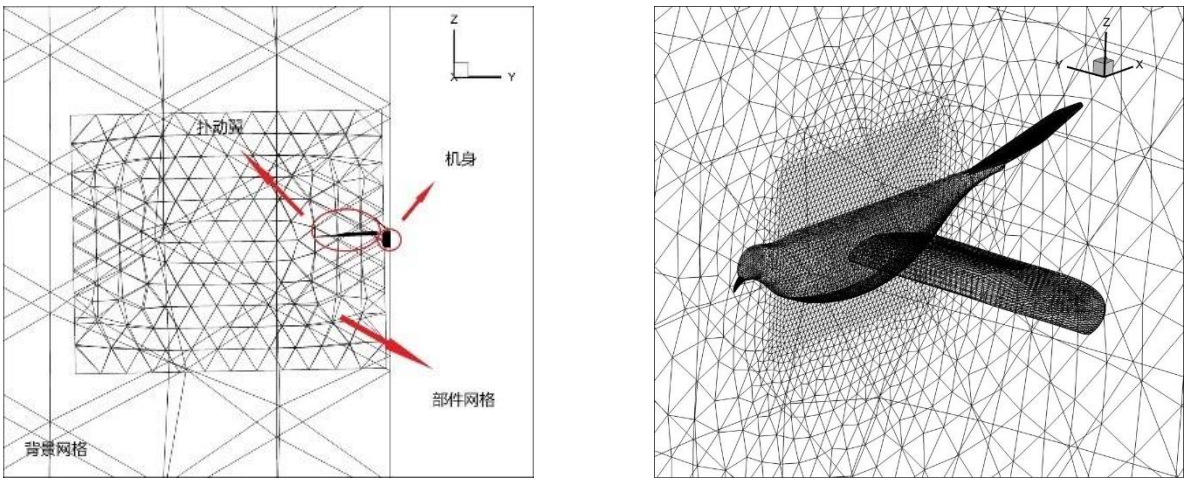

(a) overall grid strategy (b) wing surface mesh and dense region

Figure 5 – Mesh strategy for the flexible wing: (a) overall grid strategy; (b) wing surface mesh and dense region.

3. Results and Discussions

3.1 Grid convergence study

It is important to investigate the convergence of the solution with increasing grid resolution and decreasing time-step size. Therefore, to determine the proper grid resolution for the wing, a grid-convergence study is conducted for the flexible wing by varying the cell amount of the component mesh, that is, the mesh surrounds the flapping wing. As shown in Table 1, three sets of meshes were selected using different resolutions, i.e., around 2 million, 4 million, and 8 million respectively. Note that, as the dynamic morphological data acquired by the experiment was used to move the flapping-wing meshes (500 steps in one period), we thereby only test the spatial convergence accordingly.

Table 1 – Mesh resolution used in grid convergence study

Mesh resolution	Coarse	Medium	Fine
Wing surface mesh	32,000	60,000	117,000
Component mesh	1.5million	2.9million	6.4million
Background mesh	0.9million	1.1million	1.2million
Total mesh	2.4million	4.0million	7.6million

The force differences of the three sets of meshes mainly occur at the peaks and troughs of the

curves, where the wings undergo a significant unsteady aerodynamic effect.The maximum disparity of the force curves between the medium case (adopted in this paper) and the fine case is about 2%, indicating that the aerodynamic force results in the current study were grid-independent.

3.2 Force comparison of rigid and flexible wings

The resulting aerodynamic forces as well as the pressure distribution and vortex structures, are addressed and discussed in this section. In Figure 6, force coefficient variation for the two configuration (rigid and flexible) in different directions during one flapping cycle are shown. The force component in the z direction for the two configuration have a similar trend of variation. The amplitude of the two configuration is similar, but the phase is different, this may be caused by the wing flexibility. In regard to force component in the x direction, which corresponding to the thrust, the flexible wing generate considerable thrust, while the rigid wing model generate almost no thrust. This is foreseeable because the flexible case tend to form a pitching angle during the flapping cycle, which is beneficial for thrust generation.

Under current flow conditions (no incoming flow), from an analytical point of view, the thrust will be essentially zero, if the wings are rigid. With the absence of incoming flow, the airflow does not deflect due to the flapping itself, and the rigid wing does not allow to exhibit a spanwise twist (pitching in 2D airfoil), and the resulting force will be mainly point to the z direction. There will be almost no component in the thrust direction. In the real wing case, the wing flexibility allows spanwise twist, this produces a pitching effect at the wing sections so that thrust can be generated even without incoming flow.

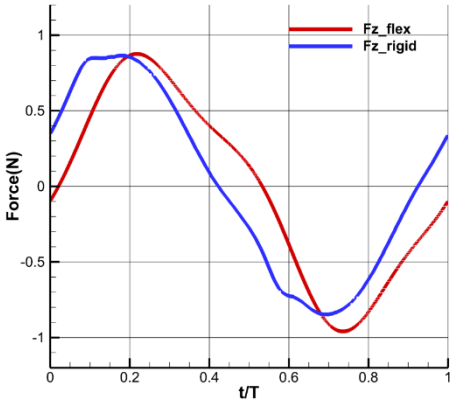

(a) forces in the vertical direction

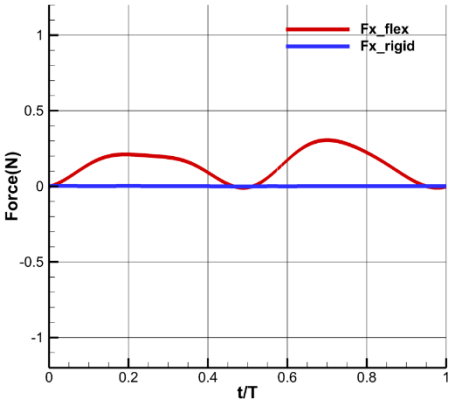

(b) forces in the horizontal direction

Figure 6 – Force comparison of rigid and flexible wings in the: (a) vertical direction and (b) horizontal direction.

3.3 Aerodynamics and flow structures

Figure 7 shows the instantaneous pressure contours at t/T=0.00, t/T=0.25 (halfway downstroke), t/T=0.50, and t/T=0.75 (halfway upstroke). At t/T=0.25, there is a significant low-pressure area on the upper surface of the wing due to the leading edge vortex, while a relatively uniform high-pressure area on the lower surface due to impacting with the air, as clearly shown in Figure 7b. Similarly, at t/T=0.75, the relatively uniform high-pressure area is switched to the upper surface, while the low-pressure area caused by the leading edge vortex during upstroke presents in the lower surface, as shown in Figure 7d. The net pressure difference between the upper and lower surfaces at these two moments are the main reason for the extremum values at these two moments.

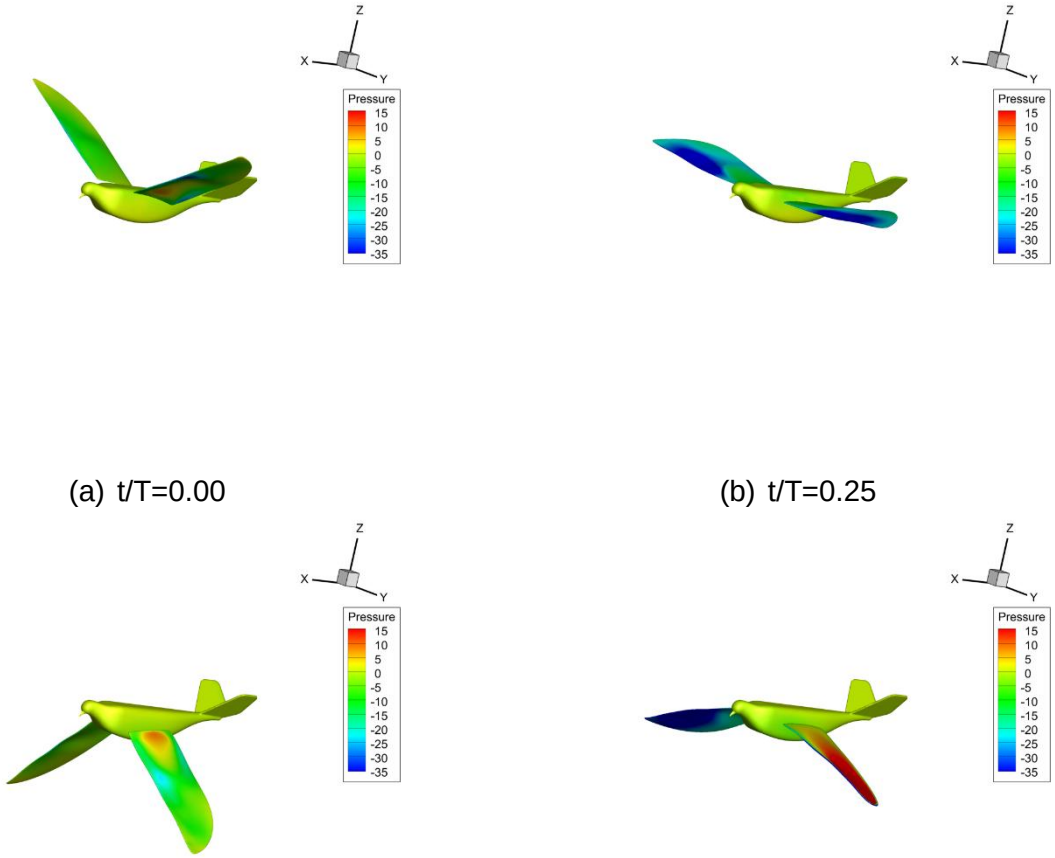

(a) t/T=0.00 (b) t/T=0.25

(c) t/T=0.50 (d) t/T=0.75

Figure 7 – Pressure distribution at: (a) beginning of downstroke; (b) middle of downstroke; (c) beginning of upstroke; (d) middle of upstroke.

In order to further analyze the flow structures around the wing, the vortex structures at different moments are visualized by using the Q criterion,[21] which are colored by y vorticity for defining the rotational direction (seen in Figure 8). There are four dominant vortex structures: the Leading Edge Vortex (LEV), the Trailing Edge Vortex (TEV), the Tip Vortex (TV), and the vortex ring. Note that the vortex ring is jointed by the LEV, TV, and TEV.

At t/T=0.0, when it is at the start of the downstroke, the LEV, TEV, and the TV that are generated during the previous upstroke are about to shed from the wing to prepare for the generation of new vortexes. Consider that, if the wing is rigid, the vortex system in the early downstroke should be generated due to the still rising airflow. However, because of the presence of deformation on the real wing, the outer part of the wing is still moving upward, and the early vortex system is delayed compared with the rigid wing.

At t/T=0.1, a vortex ring is generated on the upper surface of the wing and becomes larger with the flapping goes on. The vortex ring, which is jointed by the edge vortexes (i.e., LEV, TEV, and TV), is observed to become stronger until the wing rotates to the extreme position where the downstroke ends and the upstroke starts. From t/T=0.1 to t/T=0.5, the vortex ring forms and stretches around the wing and eventually breaks down.

At t/T=0.5, when the upstroke starts, the vortex structures generated during downstroke are not completely detached due to the still downward-moving outer wing part. Shortly after t/T=0.5, the whole wing flaps up and new vortexes are generated. The following process is similar to that of the downstroke.

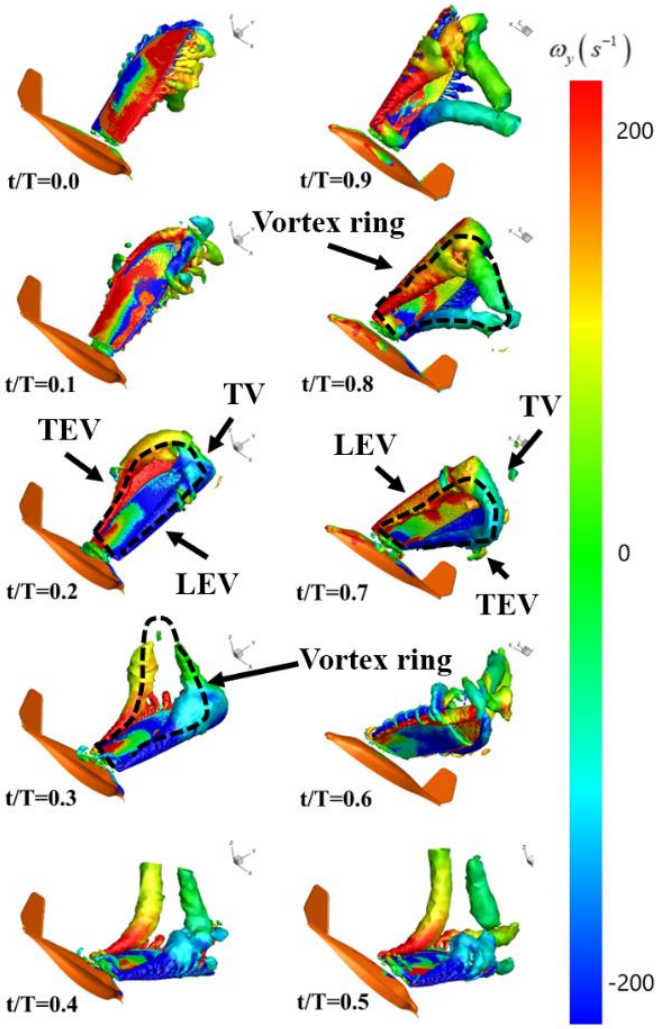

Figure 8 – Isosurface of Q criterion (Q=5000) colored by y vorticity during one flapping cycle.

4. Conclusions

The aerodynamic characteristics of a flexible flapping wing were numerically simulated using ANSYS Fluent. To accurately model the kinematics of the flexible flapping wing, the morphological deformation pattern derived from a photogrammetry experiment was used as a prescribed input to the solver, thus omitting the need for a complex FSI model. The results shows that the flexible case tend to form a pitching angle during the flapping cycle, which is of benefit to thrust generation. The following conclusions can be drawn from the study:

(1)The formation and evolution of the vortical structures, including the LEV, TEV, TV, and vortex rings, are visualized by the CFD simulation. In the middle of the downstroke, there is a noticeable low-pressure area on the upper surface of the wing due to the LEV, while a relatively uniform high-pressure area on the lower surface due to impacting with the air. The net pressure difference between the upper and lower surfaces at t/T=0.25 and t/T=0.75 is the main reason for the extremum values at these two moments. The vortex ring is formed by the LEV, TV, and TEV according to the theory of vortex dynamics which states that vortex filaments can only end at solid walls or form vortex rings. Because the numerical simulation is carried out under the condition of zero freestream velocity, the vortical structures are advected only by self-induction, and hence tend to stick near the wing, resulting in a complex interference structure around the wing.

(2)From an analytical point of view, the thrust will be essentially zero, if the wings are rigid. With the absence of incoming flow, the airflow does not deflect due to the flapping itself, and the rigid wing does not allow to exhibit a spanwise twist (pitching in 2D airfoil), and the resulting force will be mainly point to the z direction. There will be almost no component in the thrust direction. In the real wing case, the wing flexibility allows spanwise twist, this produces a pitching effect at the wing sections so that thrust can be generated even without incoming flow.

This study is helpful for understanding the effect of wing flexibility and gives new insights into the

three dimensional vortex structure in the vicinity of the flexible wing.

Copyright Statement

The authors confirm that they, and/or their company or organization, hold copyright on all of the original material included in this paper. The authors also confirm that they have obtained permission, from the copyright holder of any third party material included in this paper, to publish it as part of their paper. The authors confirm that they give permission, or have obtained permission from the copyright holder of this paper, for the publication and distribution of this paper as part of the ICAS proceedings or as individual off-prints from the proceedings.

References

[1] Shyy W, Aono H, Chimakurthi SK, et al. Recent progress in flapping wing aerodynamics and aeroelasticity. *Prog Aerosp Sci* 2010;46(7):284–327.

[2] Weis-Fogh T. Quick Estimates of Flight Fitness in Hovering Animals, Including Novel Mechanisms for Lift Production. *J Exp Biol* 1973;59(1):169-230.

[3] Dickinson M. The effects of wing rotation on unsteady aerodynamic performance at low Reynolds numbers. *J Exp Biol* 1994;192(1):179-206.

[4] Ellington C P, van den Berg C, Willmott A P, et al. Leading-edge vortices in insect flight. *Nature* 1996;384(6610):626-630.

[5] Keennon M, Klingebiel K, Won H. Development of the nano hummingbird: A tailless flapping wing micro air vehicle. 50th AIAA aerospace science meeting. Reston: AIAA; 2012.

[6] Ma K Y, Chirarattananon P, Fuller S B, et al. Controlled Flight of a Biologically Inspired, Insect-Scale Robot. *Science* 2013;340(6132):603.

[7] Karasek M, Muijres F T, De Wagter C, et al. A tailless aerial robotic flapper reveals that flies use torque coupling in rapid banked turns. *Science* 2018;361(6407):1089-1094.

[8] Deng S, Percin M, van Oudheusden B W, et al. Numerical Simulation of a Flexible X-Wing Flapping-Wing Micro Air Vehicle. *AIAA J* 2017;55(7):2295-2306.

[9] Dong X, Li D, Xiang J, Wang Z. Design and experimental study of a new flapping wing rotor micro aerial vehicle. *Chin J Aeronaut* 2020.

[10]Chen L, Zhang Y, Chen Z, et al. Topology optimization in lightweight design of a 3D-printed flapping-wing micro aerial vehicle[J]. *Chin J Aeronaut* 2020,33(12):3206-3219.

[11]Yang W, Wang L, Song B. Dove: A biomimetic flapping-wing micro air vehicle. *Int J Micro Air Veh* 2017;10(1):70-84.

[12]Yang W, Song B, Song W, et al. The effects of span-wise and chord-wise flexibility on the aerodynamic performance of micro flapping-wing. *Chinese Science Bulletin* 2012;57(1001-6538):2887.

[13]Xue D, Song B, Song W, et al. Effect of wing flexibility on flight dynamics stability of flapping wing MAVs in forward flight. *Int J Micro Air Veh* 2016;8(3):170-180.

[14]Xue D, Song B, Song W, et al. Computational simulation and free flight validation of body vibration of flapping-wing MAV in forward flight. *Aerosp Sci Technol* 2019;95:105491.

[15]Zhou C, Zhang Y, Wu J. Aerodynamic periodicity of transient aerodynamic forces of flexible plunging airfoils[J]. *Chin J Aeronaut* 2021,34(1):10-21.

[16]Zhou C, Zhang Y, Wu J. Effect of flexibility on unsteady aerodynamics forces of a purely plunging airfoil[J]. *Chin J Aeronaut* 2020,33(1):88-101.

[17]Li Z, Feng L, Wang J. Individual influence of pitching and plunging motions on flow structures over an airfoil during dynamic stall[J]. *Chin J Aeronaut* 2020,33(3):840-851.

[18]Lang X, Song B, Yang W, et al. Aerodynamic performance of owl-like airfoil undergoing bio-inspired flapping kinematics[J]. *Chin J Aeronaut* 2021,34(5):239-252.

[19]Tay W, Jadhav S, Wang J. Application and Improvements of the Wing Deformation Capture with Simulation for Flapping Micro Aerial Vehicle[J]. *J Bionic Eng* 2020,17(6):1096-1108.

[20]ANSYS Fluent User's Guide for Release 19.2, 2018.

[21]Hunt, J. C. R., Wray, A. A., Moin, P. Eddies, Streams, and Convergence Zones in Turbulent Flows Proceedings of the Summer Program, Center for Turbulence Research 1988, pp. 193–208.